MATERIALS SCIENCE

Aberration-corrected STEM imaging of 2D materials: Artifacts and practical applications of threefold astigmatism

Sergei Lopatin[1]*†, Areej Aljarb[2,3,4]*, Vladimir Roddatis[5], Tobias Meyer[6], Yi Wan[2], Jui-Han Fu[2,3], Mohamed Hedhili[2], Yimo Han[7], Lain-Jong Li[2], Vincent Tung[2,3]†

High-resolution scanning transmission electron microscopy (HR-STEM) with spherical aberration correction enables researchers to peer into two-dimensional (2D) materials and correlate the material properties with those of single atoms. The maximum intensity of corrected electron beam is confined in the area having sub-angstrom size. Meanwhile, the residual threefold astigmatism of the electron probe implies a triangular shape distribution of the intensity, whereas its tails overlap and thus interact with several atomic species simultaneously. The result is the resonant modulation of contrast that interferes the determination of phase transition of 2D materials. Here, we theoretically reveal and experimentally determine the origin of resonant modulation of contrast and its unintended impact on violating the power-law dependence of contrast on coordination modes between transition metal and chalcogenide atoms. The finding illuminates the correlation between atomic contrast, spatially inequivalent chalcogenide orientation, and residual threefold astigmatism on determining the atomic structure of emerging 2D materials.

INTRODUCTION

In contrast to graphene, monolayer two-dimensional (2D) transition metal dichalcogenides (TMDs) exhibit different polymorphs—that is, more than one crystal structure exists. Different crystalline structures of 2D TMDs directly reflect changes in electronic properties, the ability to transport carriers, propensity toward chemical synthesis, and capability to drive catalytic reactions (*1*, *2*). Unraveling the structure-property-performance relationship requires an advanced characterization tool at their native length scales. Imaging characterizations by means of high-resolution scanning transmission electron microscopy (HR-STEM) are gaining unmatched spatial resolution with the development of spherical aberration (Cs) correctors (*3*, *4*). In particular, HR-STEM coupled with the annular dark-field (ADF) detector, especially in the regime of nearly quadratic dependence of the image contrast on the atomic number (Z-contrast), provides straightforward in situ visualization of the coordination of constituent atoms (*5*). Brighter spots in atomic-scale Z-contrast images of crystalline materials can be directly translated into heavier atoms and vice versa (*6*, *7*). The discovery of nonmonotonic Z dependence, however, raises uncertainty with varying levels of complexity (*8*). To prevent the structural misinterpretation of the imaging results requires the integration of the "full package" of model-simulation-experiment pathways (maybe in several iterations), even for Z-contrast HR-STEM (*9*).

Whereas recent technological advances in the electron-optics design for high-end HR-STEMs (*10*) have largely negated the adverse effect of dominant aberrations, i.e., Cs of the third order, it remains an open question on how the combination of chromatic aberration (Cc), the fifth-order Cs, and nonrotationally symmetric residual aberrations, especially at lower accelerating voltage (*11*), weighs in and becomes detrimental to the overall (S)TEM resolution (*12*, *13*). From a theoretic perspective, reaching the highest spatial resolution in STEM requires an electron beam (probe) of an infinitely small size. In practice (because of natural physical limits) (*11*), this is not achievable, and the real electron probe has a definite size, which can be interpreted into the resolution power of a particular STEM instrument.

In modern systems, the probe size can be reduced below 0.1 nm, enabling sub-angstrom (*14*) and even sub–50-pm (*15*) resolution for bulk samples and the record-breaking resolution of 0.4 Å (*16*) for 2D materials. If, at the same time, the probe shape (the beam cross-section intensity distribution) is not spherical but rather triangular in profile, this is described as a threefold electron probe astigmatism, often termed as A2 (or a33 in equivalent), where the number stands for the second order of that residual aberration. The value of A2 is measured in nanometers. STEMs produced by mainstream manufactures are typically equipped with probe Cs-correctors that minimize the A2 below 100 nm, which is considered acceptable.

There are reports with better numbers for A2; however, these numbers are not substantiated by a rigorous measurement that involves statistically significant repetitions and accuracy evaluation. Rather, A2 is obtained from a one-time measurement provided by the corresponding software, which feeds back only the confidence level. This unsystematic approach can lead to unintended consequences that always create considerable scatter in data, a detriment to evaluating the accuracy. Moreover, for the majority of the STEM systems, the measurement and aberrations tuning algorithm depend

---

[1]King Abdullah University of Science and Technology (KAUST), Core Labs, Thuwal 23955-6900, Saudi Arabia. [2]Physical Science and Engineering Division, King Abdullah University of Science and Technology (KAUST), Thuwal 23955-6900, Saudi Arabia. [3]Physical Science and Engineering Division, King Abdullah University of Science and Technology (KAUST), KAUST Solar Center, Thuwal 23955-6900, Saudi Arabia. [4]Department of Physics, King Abdulaziz University, Jeddah 23955-6900, Saudi Arabia. [5]Institute of Materials Physics, University of Goettingen, Goettingen, Germany. [6]4th Institute of Physics - Solids and Nanostructures, University of Goettingen, Goettingen, Germany. [7]Department of Molecular Biology, Princeton University, NJ 08544-1044, USA.
*These authors contributed equally to this work.
†Corresponding author. Email: sergei.lopatin@kaust.edu.sa (S.L.); vincent.tung@kaust.edu.sa (V.T.)

on the dedicated alignment of the sample, which is extracted from the microscope before proceeding to the "real" specimen, i.e., the one being actually investigated under STEM. Meanwhile, the value of A2 is known to drift significantly during the course of the characterization and can be influenced easily even through the exchange of specimens.

The effect of electron beam shape on the imaging of 2D layered materials was first mentioned by Krivanek *et al.* (*17*). In this seminal work, they demonstrated the unmatched ability to commence an atom-by-atom chemical analysis with HR-STEM ADF in 2D layered materials. In particular, the residual aberrations (especially aberrations with the same symmetry as the structure being imaged) can lead to contrast artifacts as a result of the probe "tails" to the intensity recorded at the nominal probe position (*18*–*20*). This profound effect of residual aberrations on HR-TEM imaging is also discussed in a number of publications (*12*, *13*, *21*–*23*). However, most of these studies, both for HR-TEM and HR-STEM, predominately focused on graphene, a monolayer of carbon atoms exclusively. This variation in imaging analysis may not cause significant uncertainties when monolayer graphene is being investigated. However, the misinterpretation in imaging analysis can be adverse when 2D monolayer TMDs, which, itself, contains three layers of atoms and can be polymorphic in nature, such as molybdenum disulfide (MoS_2).

Here, the electron beam can be deemed as electromagnetic waves with rotation frequency, e.g., threefold astigmatism. The interaction with 2D monolayer TMDs is a consequence of specific phase relationships. When the spatial frequency of the incoming electron beam is "in-phase" with the 2D monolayer TMDs, the tails of the electron beam come across the relatively heavy atoms. The resultant resonant enhancement gives rise to the atomic contrast that scales roughly as the square of the atomic number Z. Meanwhile, other phase relationships are possible between the electron beam and 2D materials that will not lead to this resonant enhancement. When the electron beam is "out-of-phase"—that is, the tails of the electron beam do not constructively interfere/distribute with the 2D monolayer materials—the result is the contrast damping (antiresonance). It is thus apparent that variation in electron beam orientation can be used to "modulate" the contrast between dissimilar atoms. Together, we term the finding resonant modulation of contrast (RMC) as a recognition that contrast of metal and chalcogenide atoms in HR-STEM images can be modulated by varying the rotation frequency of incoming electron beams.

Here, we report the correlation of atomic simulation packages with HR-STEM ADF imaging to reveal the false T phase of TMDs as a result of the residual threefold astigmatism, where its tails can overlap and thus interact with several atomic species simultaneously. This false phase is particularly pronounced for materials made of different atomic species, which arises and then follows a threefold (120°) in-plane rotation symmetry of its origin (i.e., A2). Depending on the mutual orientation between A2 and the specimen inside the HR-STEM, atomic-scale imaging of the same 2D monolayer TMDs can result in a manually variable contrast, leading to a violation of power-law dependence on atomic number and thus alteration of crystal structure interpretation. Both theoretical simulation and experimental observation suggest that RMC arises even when A2 is around 100 nm and adversely affects the fidelity of structural analysis of 2D monolayer TMDs.

While the advent of an aberration-corrected HR-STEM ADF represents a very powerful yet general analysis tool to determine structural evolution in both real-time and atom-by-atom manners, the combined simulation and experimental characterizations in imaging analyses allows us to determine the origin and then address the adverse impact of RMC. A viable solution emerges to negate the adverse effect through the employment of an electron beam monochromator, which can achieve an energy spread below 60-meV resolution (*24*–*27*), thus mitigating the RMC below the detection limit and to image 2D TMDs without artifacts regardless of the sample orientation or A2 (up to 150 nm) rotation.

RESULTS

TMD mirror grain boundary: A model system

To demonstrate the RMC, we used 2D monolayer MoS_2 as a representative model system, which is known for exhibiting a variety of polymorphs because an individual MoS_2 monolayer, which, itself, comprises three layers of atoms (S-Mo-S), can be in either one of the two phases, namely 2H and 1T polymorphs (fig. S1). Although both domains in the mirror grain boundaries are made of intrinsic 2H phases, S orientation with respect to Mo on both domains is not spatially equivalent as shown in Fig. 1A. On the left-hand side, namely LHS, of the model, each pair of S atoms adjacent to Mo in the vertical direction is located above the Mo. For clarity, we denote such a configuration as 2H (S↑) and mark it with the green arrow up. On the right-hand side, termed RHS, the orientation is reversed, where two S atoms are now positioned below Mo. Therefore, this is assigned as the 2H (S↓) configuration, highlighted with the green arrow down. The 2H (S↑) and 2H (S↓) configurations are differentiated only by a 60° or 180° in-plane rotation. This inequivalence in the in-plane orientation provides a well-defined model system that gives rise to a stark atomic contrast in ADF imaging between opposite domains. Such a model of 2H (S↑)-2H (S↓) mirror grain boundary corresponds to the typical growth orientation mismatch in monolayer MoS_2 films grown by chemical vapor deposition (CVD) (*28*).

Because A2 is the aberration with a strong rotation anisotropy, it is assumed that imaging artifacts will hinge strongly on the orientation of the specimen relative to A2. For the clarity of notation, the orientation of A2 (with respect to the model structure) with one of the corners pointing up is defined as (A2↑). The orientations of (A2↑) and (A2↓) are the result of 60° rotation, while rotating by 30° affords (A2←) and (A2→). The relative magnitude of A2 increases with increasing lengths of red arrows. Depending on the mutual orientation between MoS_2 and A2, RMC could arise and influence the imaging results and hence the structural interpretation as shown in Fig. 1 (B and C).

Simulation

As a first step in investigating the role of RMC in the imaging of 2D monolayer MoS_2, Dr. Probe (*29*) and QSTEM (*30*) software packages were used to simulate HR-STEM ADF of the mirror grain boundary, across which spatial orientations alter, e.g., 2H (S↑)-2H (S↓) (Fig. 2A). Conditions implemented are based on the model in Fig. 2B, for the case of Cs = 1 μm and all the residual aberrations, including A2, set to zero. On both sides of mirror grain boundary, S and Mo atoms are clearly resolved: Three Mo atoms coordinated with three pairs of S atoms form a sixfold ring, characteristic of the 2H phase. Next, we gradually (50-nm increment) increase A2 in our simulations. The effect of A2 on the electron beam shape is shown in the insets of Fig. 2 (A and D to L). For A2 = 0 nm, nearly all electrons

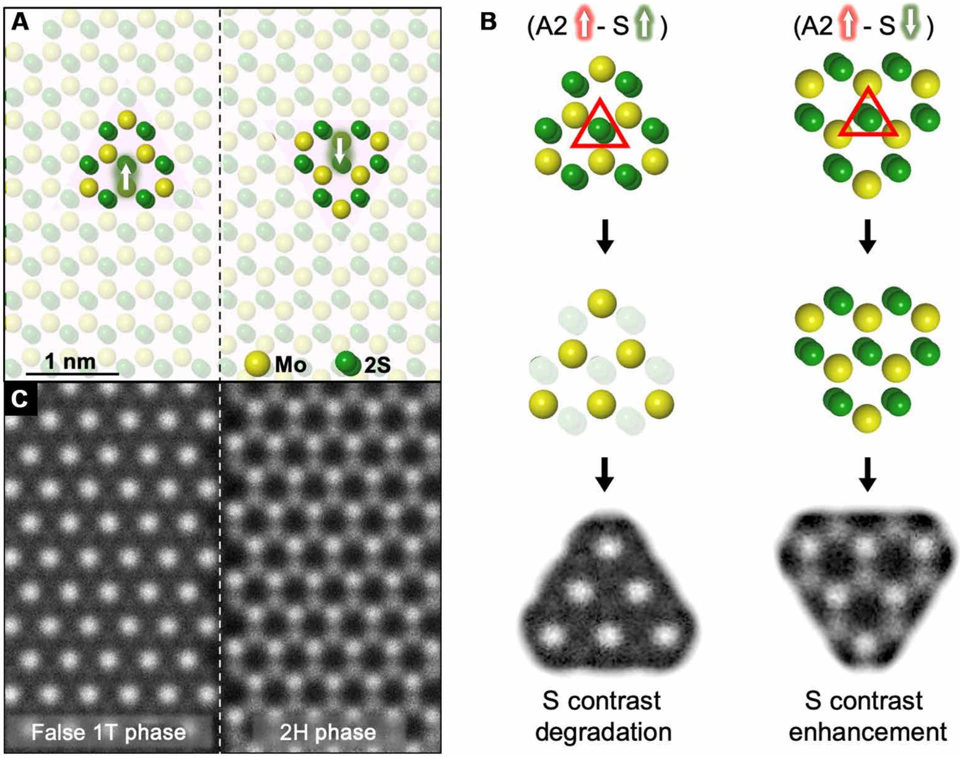

Fig. 1. Schematic illustration of the emergence of RMC as a result of the mutual orientations between A2 (red arrows) and MoS_2 (green arrows). (**A**) Computer-generated atomic models of monolayer MoS_2 with a mirror grain boundary. (**B**) Schematic representations of the dissimilar atomic configurations where S contrast degrades on LHS, and enhancement in S contrast is observed on RHS. (**C**) Simulation of HR-STEM ADF imaging for the atomic models in (A) with A2 applied.

are concentrated at the center of the beam, giving rise to a round-shaped probe. With increased magnitude of A2, significant numbers of electrons are redistributed toward the tails, resulting in a triangular-shaped and much bigger probe. Our simulations reveal that increasing a threefold astigmatism in the orientation (A2↓) on the RHS (S↓) is manifested in the dominant emergence of Mo atoms, while the contrast of S atoms drastically decreases (Fig. 2, D to F), compared with the LHS (S↑). Already, at A2 = 100 nm, the contrast of S on the (S↓) side nearly vanishes. Meanwhile, in the case of RHS (S↓) shown in Fig. 2 (E and F), the "visual transition" from the 2H (S↑)-2H (S↓) mirror grain boundary to the 2H - false 1T (false 1T refers to 1T-like phase caused by the RMC) phase boundary takes hold at A2 = 150 nm, closely resembling the intrinsic 1T or "S contrast degradation" often reported for the metallic 1T MoS_2.

As indicated in the model in fig. S1B, each S site in the projection of the 2D crystal lattice comprises only one atom (as opposite to the 2H phase with two S atoms in the same projection) whose exceedingly low signal-to-noise ratio makes it indiscernible from HR-STEM ADF imaging, leaving behind discernable patterns of Mo atoms. While such a glaring contrast in HR-STEM ADF imaging has long been used to unambiguously distinguish these chemically homogeneous but crystallographically heterogeneous phases, it becomes a formidable challenge to determine a given domain whether it is an artificially false 1T or an intrinsically metallic 1T phase. As schematically represented in Fig. 2C, when the electron probe (red triangle) is arranged in the (A2↓ - S↑) configuration, the threefold tails of the probe are found to overlap with the neighboring Mo atoms and hence lead to stronger scattering of the electron beam. The scatter in the electron beam is a consequence of the heavier Mo atoms—that is, higher contrast in HR-STEM ADF. Even a small portion of the beam (tails) scattered at this position by Mo atoms will inevitably add up to the S signal, concurrently enhancing the effective contrast of (S↑) atoms in LHS (Fig. 2, D to F) and thus the emergence of the 2H phase.

On the other hand, for the (A2↓ - S↓) configuration (Fig. 2C), when the electron probe is placed on S, its tails will not interfere with Mo atoms, and thus, no enhancement in S contrast is observed. Similar to the intrinsic 1T phase, this lack of enhancement of S contrast also renders S "invisible," leading to the inception of a false 1T type of contrast. Likewise, visual transition from false 1T→2H is demonstrated in Fig. 2 (G to I) when reversing the direction of A2 (A2↓ to A2↑) while keeping the S configuration constant. Meanwhile, it is also noted that there is an intermediate state (A2←) or (A2→), for which contrast of S atoms degrades (because of the effectively bigger probe) equally on both sides of the domains (Fig. 2, J to L). Drawing on these simulation results, a picture emerges indicating that RMC of lighter elements, where electron probe tails intersect neighboring heavier atoms, comes into effect when threefold astigmatism is in the range of 100 to 150 nm coupled with the direction of A2 relative to the crystal structure orientation.

Experiment

To confirm the predictions from QSTEM simulations, 2D monolayer MoS_2 with a 2H (S↑)-2H (S↓) mirror grain boundary with a 60° growth mismatch (see Supplementary Text) was synthesized via CVD. HR-STEM ADF imaging was performed to resolve the atomic structures specifically on regions separated by a sharp grain boundary with the following conditions: (i) manual in-plane rotation of the

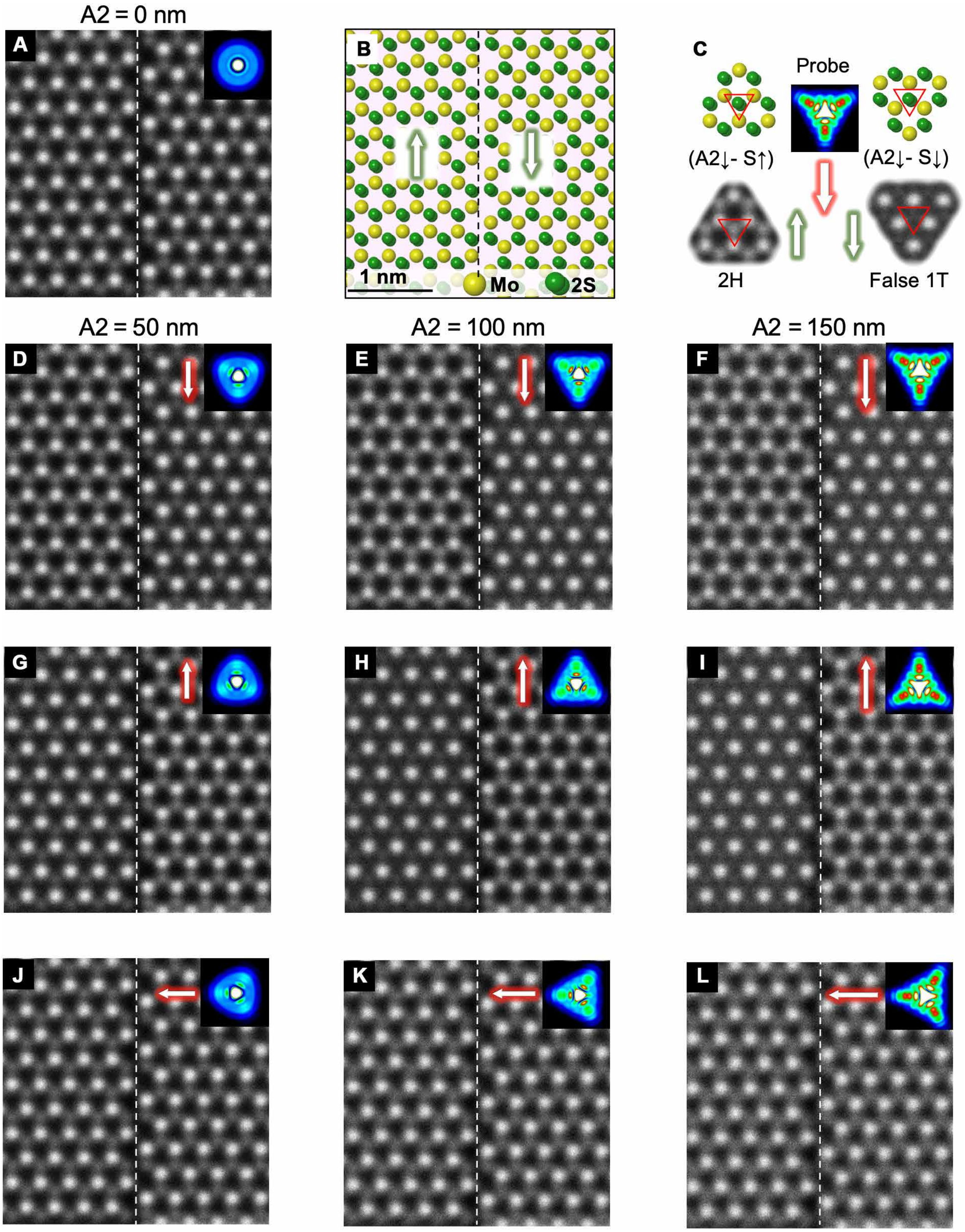

Fig. 2. QSTEM simulation of HR-STEM ADF imaging. Domains of 2D monolayer MoS_2 separated with an antiphase (60° or 180° in-plane rotation) growth mismatch for Cs-corrected electron probe with various A2. (**A**) Image taken from QSTEM simulation based on the atomic model in (**B**) with A2 = 0 nm. (**C**) Schematics of A2 orientation effect on S contrast. (**D** to **L**) Same as in (A) but with different values and orientations of A2 introduced. Insets in (A) and (D) to (L) show the relative magnitude and orientations of A2 (red arrows) and the attendant evolution of the electron probe shape.

2H MoS_2 specimen inside the TEM holder for otherwise fixed microscope conditions, followed by (ii) imposing and rotating a threefold astigmatism with respect to a fixed sample orientation. To this end, we first focused on regions in the vicinity of the mirror grain boundary where the two MoS_2 domains intersect as schematically illustrated in Fig. 3.

First, TEM holder was rotated clockwise in situ with a 10° increment until the RMC is at its peak on one side, and hence, false 1T

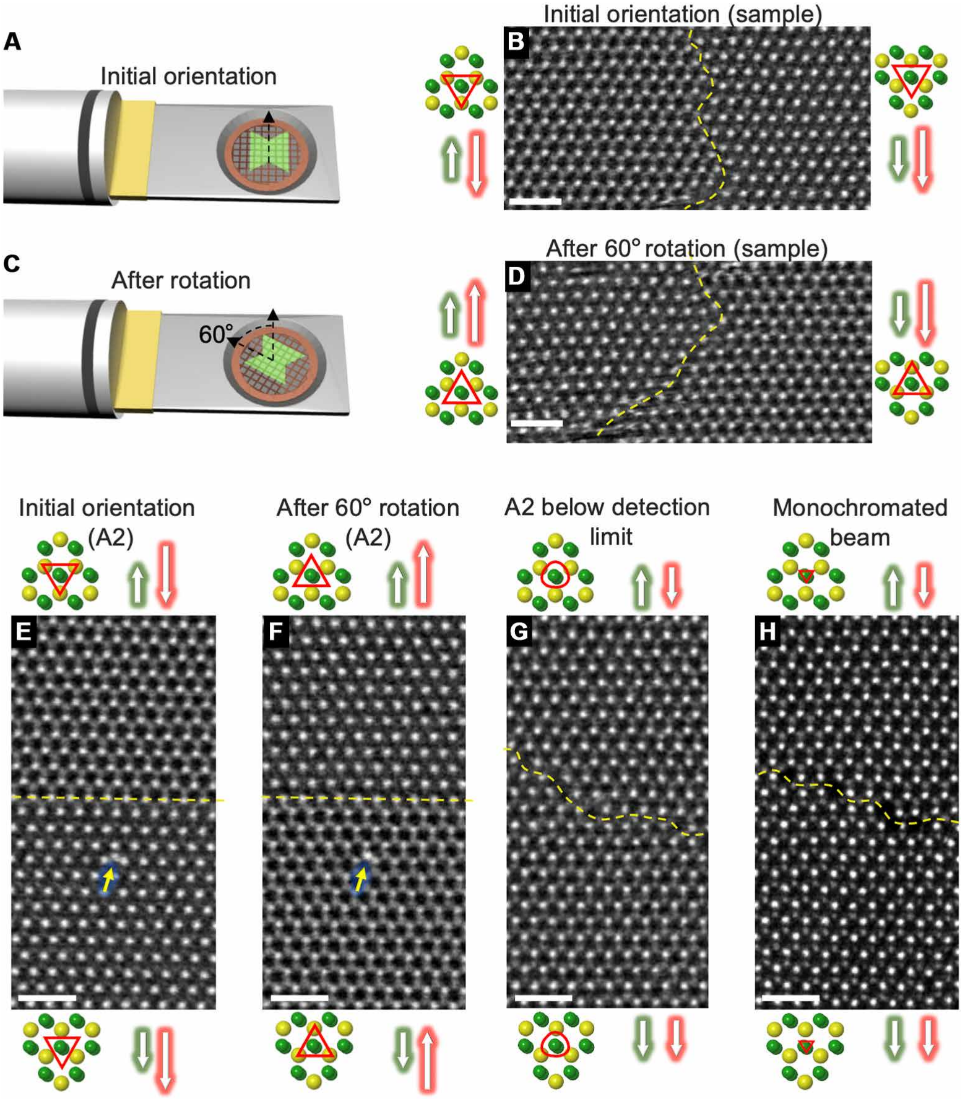

Fig. 3. Experimental observations of RMC in HR-STEM ADF imaging. (**A** to **D**) Sample rotation experiment: HR-STEM ADF imaging taken at regions in close proximity to the interface between MoS_2 mirror grains with an antiphase (60°) growth mismatch. Schematic representation of the relative position of sample supported on TEM holder before and after rotation is illustrated in (A) and (C). Corresponding HR-STEM ADF images before and after an in-plane rotation by 60° are shown in (B) and (D). The experimental observation agrees very well with the QSTEM simulation results as is evident by the atomically resolved phase transition after A2 rotation. (**E** to **H**) A2 rotation experiment: Cs-corrected HR-STEM ADF imaging of the interface between a monolayer MoS_2 grains with antiphase (60°) growth mismatch. (E and F) Images at the same spot of the interface before and after A2 = 100-nm rotation by 60°, correspondingly. Atomic models (yellow for Mo and green for S) and arrows (green for sulfur and red for A2) suggest A2 orientation based on the simulation in Fig. 2. (G) Image of the interface for A2 reduced below the detection limit, and (H) additionally, monochromated beam (60-meV energy spread) was used. Scale bars, 1 nm.

phase is observed. As indicated in Fig. 3B, the domain on LHS (S↑) is characterized by the trigonal prismatic coordination, e.g., 2H phase, whereas the significantly reduced contrast of S atoms on RHS (S↓) appears as the false 1T when A2 is applied. The presence of 2H—false 1T polymorphs matches well with the simulation results shown in Fig. 2 (E and F). After manually rotating the double-truncated MoS_2 specimen by 60° counterclockwise (Fig. 3C), we again observed a reversion to the false 1T—2H polymorphs as is evident in Fig. 3D. The reversion of contrast that alternates in every 60° increment confirms the threefold symmetry of the RMC. These observations are in good agreement with theoretical modeling and therefore allow us to determine the orientation of A2 during the HR-STEM ADF imaging.

Another important factor that weighs in the visual transition between 2H and false 1T is the direction of A2. Here, we rotated the direction of A2 through the assistance of a Cs-probe corrector software (see details in the Supplementary Materials) until the maximum RMC was achieved and hence the emergence of visual transition from 2H→false 1T. As shown in Fig. 3E, the 2H domain (S↑) above the abrupt phase boundary is unambiguously juxtaposed with the false 1T phase in the bottom domain (S↓), corroborating the existence of RMC. In the next step, A2 is rotated by 180° (60°). Such a rotation of A2 results in the inversion of the contrast across phase boundary and thus reverses the phases on both domains as demonstrated in Fig. 3F.

Meanwhile, point defects in CVD-grown MoS_2, including substitutional, interstitial atoms, and vacancies, have been reported by several groups and are known to induce pronounced structural distortions as highlighted with yellow arrows in Fig. 3 (E and F). If phase transformation truly took place, top and bottom planes of S atoms are forced to shift away. This may, in turn, propel structural defects deviated away from their origins slightly, although a more vigorous investigation is required. We surmise that point defects should persist if phase reversion is truly artificial in nature as opposed to rearrangement of lattice or sliding of atomic planes. Here, the point defect is, however, found to remain still in its original position and differs only by the atomic contrast after coupling with the probe tail interaction and the presence of RMC. The persistence of point defects confirms that no major structural rearrangement or atomic displacement occurs during the A2 rotation. To further verify the influence of the magnitude of A2 on phase transition, the magnitude of A2 in Fig. 3G is reduced to 50 nm (versus 100 nm in Fig. 3E), which is below the detection limit. The influence of A2 fades quickly, and the sixfold atomic rings that constitute the 2H phase again come into sight on both domains despite the relatively low S contrast in accordance with the simulation results featured in Fig. 2A.

Mitigating the RMC

Yet, the finding here also signals the need for searching alternative ways to improve the atomic contrast and separation (i.e., resolution) without the interference of RMC. We demonstrate that the implementation of a monochromated beam can effectively address the RMC (Fig. 3H) while improving the resolution (*24*–*27*). Making use of the monochromator allows us to achieve the energy spread ΔE in the beam of ~60 meV (determined from the full width at half maximum of the zero-energy loss peak) compared to 1 eV in the original beam. With a typical value of chromatic aberration for TEM of Cc = 1.7 mm, the "energy length" parameter Cc ΔE is then maintained well under 0.1 eV mm. Consequently, the effect of chromatic aberrations of the electron-optic system is drastically reduced, allowing further demagnification of the probe while significantly improving the spatial resolution by nearly 200% (*11*) as compared between Fig. 3 (G and H, respectively).

Phase characterization

More insights into the structural continuity and chemical composition of CVD-grown MoS_2 are gained through combined spectroscopic characterizations, including photoluminescence (PL) mapping, electron energy-loss spectroscopy (EELS) bandgap measurements, and x-ray photoelectron spectroscopy (XPS). To ensure the coherence and validity of data interpretation, we directly used the same MoS_2 specimen characterized with the 2H (S↑)-2H (S↓) mirror grain boundary without post-transferring from the TEM grid. Figure S8A features an optical image of a butterfly-shaped MoS_2. The corresponding PL intensity mapping shown in fig. S8B closely resembles the optical image with a uniform yet narrow wavelength distribution intensity in both domains, indicating that both domains are indeed semiconducting (2H phase) in nature. In parallel, EELS bandgap measurement on both domains further suggests that conduction band onset arises around 1.55 eV (fig. S8C) and displays a linear increase of the intensity, which is characteristic of 2D monolayer MoS_2 (*25*). Meanwhile, XPS spectra of Mo 3d core-level electrons show two characteristic peaks assigned at 229.7 and 232.8 eV from Mo $3d_{5/2}$ and Mo $3d_{5/2}$ in Mo (IV), originating from 2H MoS_2 (fig. S8D) (*31*, *32*). Overall, these characterizations collectively confirm that both domains of the butterfly-shaped MoS_2 flake are indeed intrinsic 2H phases, and the appearance of false 1T phase is, in fact, the result of a violation of the power-law dependence of contrast on coordination modes between transition metal and chalcogenide atoms.

In addition to the mismatch in domain orientations, CVD-grown monolayer MoS_2 is also known to undergo the localized phase transformation induced by electron beams and often resolved as a 2H→1T phase transition (*33*, *34*). To discriminate the innate T phase from the false T phase, we again put the MoS_2 specimen with a 2H (S↑)-2H (S↓) mirror grain boundary into test. When applied ~100 nm of intentionally induced threefold astigmatism, LHS (A2↓ - S↑) highlighted in red shows the 2H phase, while the RHS (A2↓ - S↓) highlighted in yellow shows the false 1T phase as suggested in Fig. 4A. Aside from the mismatch of global domain orientations as shown in Fig. 2, here, we also demonstrate that local transition (embedded patch highlighted with a red color in RHS) is induced by the electron beam during the image focus optimization and twofold astigmatism adjustment. In this patch, the S atoms are clearly resolved in S↑ position [as a result of Mo plane or both S planes gliding (*34*); Fig. 4C], i.e., the patch emerges as a 2H phase and is surrounded by the matrix of a false 1T phase. Meanwhile, as A2 is deliberately rotated by 60°, the image contrast reversion again occurs universally across both domains and takes place locally at the embedded patch (Fig. 4B). Note that the patch is not only increased in dimensions by virtue of an extra beam exposure but also reverted back to the false 1T phase (now surrounded by a 2H matrix). Observing such a contrast reversion with the A2 rotation, which carries out both universally and locally, indicates that electron beam–induced 2H (S↑)→2H (S↓) transition (attributed to Mo plane or both S planes gliding) mixed with RMC are the reasons of the false 1T phase observed commonly in HR-STEM ADF images.

In addition, we demonstrate that the presence of RMC can be repurposed to facilitate the identification of S vacancies. The diminished contrast of S atoms during the RMC-driven 2H→false 1T transitions (RHS with A2↓ - S↓ configuration, the false 1T) makes the S vacancies relatively visible when compared to the original 2H phase (fig. S10). This characteristic feature combined with the intensity profile may be leveraged as a straightforward tool for revealing structural defects with vivid clarity as shown in Fig. 4 (A and B).

The combinatory studies that synergistically integrate complementary strengths from both QSTEM simulation and HR-STEM ADF imaging characterizations indicate the manifestation of RMC when the difference in atomic numbers between coordination atoms is pronounced at the presence of A2. To prove the profound and generic implication of RMC, an array of representative 2D monolayer TMDs, including WS_2, WSe_2, and graphene, have been put into test, and all of them displayed RMC-dependent atomic phase contrast albeit at various degrees (see the Supplementary Materials and figs. S11 to S18 for other systems). Moreover, false atomic contrast emanated from RMC deviates from the power-law dependence on the specimen atomic composition. This deviation from the classic power law coupled with the magnitude of A2 suggests that lighter atoms, such as Se, can appear almost as bright as nearby heavier elements (W), leading to a complete misinterpretation of HR-STEM ADF imaging results (fig. S19).

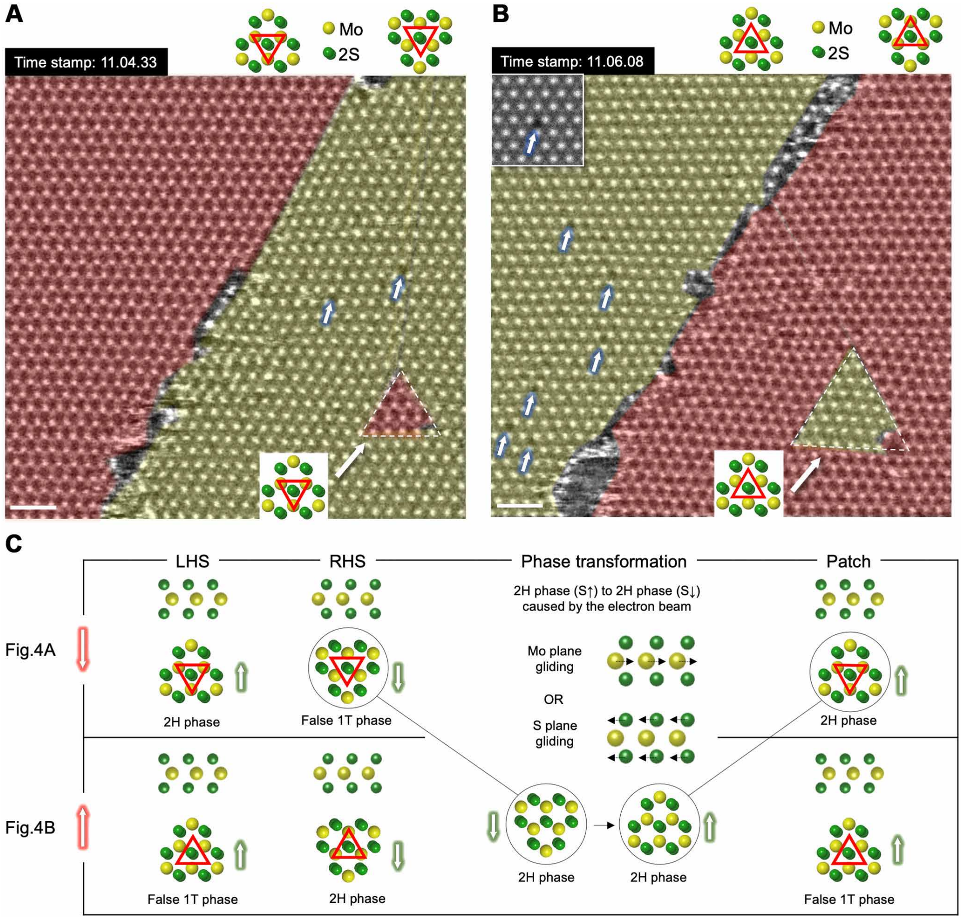

Fig. 4. Electron beam–induced local transition of embedded patch inside MoS_2 matrix. False-colored HR-STEM ADF images at a mirror grain boundary. (**A**) Before and (**B**) after A2 = 100 nm and rotating by 60°, respectively. Color coding is used to distinguish regions with 2H (red) and false 1T (yellow) types of contrast, caused by (A2↓ - S↑) and (A2↑ - S↑) imaging configuration, respectively. Red and yellow triangles in (A) and (B) show the growing 2H (S↑) transition region in 2H (S↓) matrix. Note that white arrows denote double S vacancy sites. The inset in (B) shows the simulation of false 1T contrast of MoS_2 film with a double S vacancy in the center. Scale bar, 1 nm. (**C**) Schematic representations reveal the root cause of contrast formation in both (A) and (B).

DISCUSSION

The present finding illuminates the fundamental roles of the atomic contrast, spatial inequivalent chalcogenide orientation, and residual threefold astigmatism on the determination of atomic structure of 2D monolayer TMDs. Corroborating QSTEM simulations with experimental observation of HR-STEM ADF imaging of 2D monolayer TMDs allows us to reveal the artificial nature of atomic-scale phase transitions with a relatively small amount of residual low-order aberration (A2 = 100 to 150 nm). The presence of RMC can result in artificial structures extrinsic to the specimen in HR-STEM ADF imaging both selectively and generally. These results should act as a reminder to researchers engaging in emerging 2D materials research: In addition to using HR-STEM ADF imaging to probe atomic arrangements and predict associated material properties, it is perhaps even more important to rule out the possible interference of the extended tails of threefold astigmatic electron beam that can interact with neighboring atoms to induce unwanted RMC. We suggest using more critical approaches for the interpretation of HR-STEM ADF data, especially in 2D materials. The employment of an electron beam monochromator allows us to mitigate the RMC below the detection limit and to image 2D monolayer TMDs and beyond without artifacts regardless of the sample orientation or A2 (up to 150 nm) rotation.

MATERIALS AND METHODS

Synthesis and characterizations of monolayer TMDs

MoS_2, WS_2, and WSe_2 films were grown using CVD reported previously (*28*, *35*, *36*) and were transferred onto the TEM grid by a wet transfer method. Optical images and corresponding PL mapping were collected using a Witec alpha300 confocal Raman microscope with a RayShield coupler equipped with a 532-nm wavelength laser.

High-resolution low-loss EELS

The measurements were performed at 80 kV with a Thermo Fisher Scientific USA Titan Themis Z (40 to 300 kV) TEM equipped with a high-brightness electron gun (x-FEG), an electron beam monochromator, and a Gatan Quantum 966 imaging filter (GIF). Spectra were acquired in the so-called microprobe STEM mode with about 1 mrad semi-convergence angle (4-nm probe size). The monochromator operation was optimized by the method first implemented in (*24*) and described in detail in (*25*) to achieve the energy resolution of about 45 to 50 meV (defined as the full width at half maximum of the zero-energy loss peak).

X-ray photoelectron spectroscopy

The analysis was carried out in a Kratos Axis Supra Delay-Line Detector spectrometer equipped with a monochromatic Al K_α x-ray source (hν = 1486.6 eV) operating at 150 W, a multichannel plate, and a delay line detector under a vacuum of ~10^{-9} mbar. The high-resolution spectra were collected at a fixed analyzer pass energy of 20 eV.

Image simulations

The image simulations were performed with two software packages using multi-slice methods: Dr. Probe (*29*) and QSTEM (*30*). These packages allow us to build crystal models (including artificial interfaces) using available crystallographic information files and to calculate their TEM and STEM images afterward, taking into account the various parameters of TEM (high tension, aberrations, instabilities, etc.) and the orientation of the specimen. Atomic models of synthetic grain boundaries formed by domains with a misorientation of 180° (MoS_2) and 90° (WS_2) were constructed using QSTEM Model Builder and Vesta software (*37*). We also used available DigitalMicrograph (Gatan, USA) scripts to simulate noise for the best match to experimental HR-STEM imaging. Simulation parameters were chosen as listed in table S1.

High-resolution scanning transmission electron microscopy annular dark field

HR-STEM ADF imaging was performed with a Thermo Fisher Scientific Titan Themis Z (40 to 300 kV) TEM equipped with a double Cs corrector, a high-brightness electron gun (x-FEG), and an electron beam monochromator. To reduce the electron beam sample damage, we chose to operate the microscope at 80 kV and tune it to minimize third-order Cs below the detection limit (few micrometers). However, some residual threefold astigmatism of about 100 nm (as measured by the Thermo Fisher Scientific Cs-Probe corrector software with a standard alignment sample) is intentionally left uncorrected. Images were acquired in diffraction mode with the camera length of 115 mm corresponding to the collection angles of 41 mrad (inner) and 200 mrad (outer) of a Fischione ADF detector. The probe semi-convergence angle was tuned for 30 mrad with the beam current ranging from 50 pA for the regular STEM to 3 pA for the monochromated beam STEM. For the monochromator operation, the method first implemented in (*24*) and described in detail in (*25*) was used. As a result, the monochromatic STEM was performed with the energy spread in the beam of about 60 meV (defined as the full width at half maximum of the zero-energy loss peak). Gauss high-pass (to reduce contamination effects) and low-pass (to reduce scanning noise) filtering was used to enhance the contrast of the image (figs. S2 to S6 and S12 to S16) (*15*). Measurements and calibration of optical elements of Cs probe corrector to adjust the A2 astigmatism were performed by standard Thermo Fisher Scientific software provided with a Cs probe corrector and by the use of a standard alignment sample (Cross Grating Replica 3 mm, AGS106). A Fischione Dual-Axis Tomography Holder (model 2040) was used as this holder allows the specimen to be fully rotated through 360° in the plane orthogonal to the electron beam.

SUPPLEMENTARY MATERIALS

Supplementary material for this article is available at http://advances.sciencemag.org/cgi/content/full/6/37/eabb8431/DC1

REFERENCES AND NOTES

1. G. R. Bhimanapati, Z. Lin, V. Meunier, Y. Jung, J. Cha, S. Das, D. Xiao, Y. Son, M. S. Strano, V. R. Cooper, L. Liang, S. G. Louie, E. Ringe, W. Zhou, S. S. Kim, R. R. Naik, B. G. Sumpter, H. Terrones, F. Xia, Y. Wang, J. Zhu, D. Akinwande, N. Alem, J. A. Schuller, R. E. Schaak, M. Terrones, J. A. Robinson, Recent advances in two-dimensional materials beyond graphene. *ACS Nano* **9**, 11509–11539 (2015).
2. B. Anasori, M. R. Lukatskaya, Y. Gogotsi, 2D metal carbides and nitrides (MXenes) for energy storage. *Nat. Rev. Mater.* **2**, 16098 (2017).
3. O. L. Krivanek, N. Dellby, M. F. Murfitt, Aberration correction in electron microscopy, in *Handbook of Charged Particle Optics* (CRC Press, 2008), pp. 601–640.
4. M. Haider, P. Hartel, H. Müller, S. Uhlemann, J. Zach, Current and future aberration correctors for the improvement of resolution in electron microscopy. *Phil. Trans. R. Soc.* **367**, 3665–3682 (2009).
5. S. J. Pennycook, D. E. Jesson, High-resolution Z-contrast imaging of crystals. *Ultramicroscopy* **37**, 14–38 (1991).
6. P. Y. Huang, S. Kurasch, A. Srivastava, V. Skakalova, J. Kotakoski, A. V. Krasheninnikov, R. Hovden, Q. Mao, J. C. Meyer, J. Smet, D. A. Muller, U. Kaiser, Direct imaging of a two-dimensional silica glass on graphene. *Nano Lett.* **12**, 1081–1086 (2012).
7. R. G. Mendes, J. Pang, A. Bachmatiuk, H. Q. Ta, L. Zhao, T. Gemming, L. Fu, Z. Liu, M. H. Rümmeli, Electron-driven in situ transmission electron microscopy of 2D transition metal dichalcogenides and their 2D heterostructures. *ACS Nano* **13**, 978–995 (2019).
8. S. Yamashita, J. Kikkawa, K. Yanagisawa, T. Nagai, K. Ishizuka, K. Kimoto, Atomic number dependence of Z contrast in scanning transmission electron microscopy. *Sci. Rep.* **8**, 12325 (2018).
9. R. F. Loane, P. Xu, J. Silcox, Incoherent imaging of zone axis crystals with ADF STEM. *Ultramicroscopy* **40**, 121–138 (1992).
10. B. Freitag, S. Kujawa, P. M. Mul, J. Ringnalda, P. C. Tiemeijer, Breaking the spherical and chromatic aberration barrier in transmission electron microscopy. *Ultramicroscopy* **102**, 209–214 (2005).
11. M. Haider, S. Uhlemann, J. Zach, Upper limits for the residual aberrations of a high-resolution aberration-corrected STEM. *Ultramicroscopy* **81**, 163–175 (2000).
12. J. Biskupek, P. Hartel, M. Haider, U. Kaiser, Effects of residual aberrations explored on single-walled carbon nanotubes. *Ultramicroscopy* **116**, 1–7 (2012).
13. O. Lehtinen, D. Geiger, Z. Lee, M. B. Whitwick, M.-W. Chen, A. Kis, U. Kaiser, Numerical correction of anti-symmetric aberrations in single HRTEM images of weakly scattering 2D-objects. *Ultramicroscopy* **151**, 130–135 (2015).
14. P. E. Batson, N. Dellby, O. L. Krivanek, Sub-ångstrom Resolution using aberration corrected electron optics. *Nature* **418**, 617–620 (2002).
15. R. Erni, M. D. Rossell, C. Kisielowski, U. Dahmen, Atomic-resolution imaging with a sub-50-pm electron probe. *Phys. Rev. Lett.* **102**, 096101 (2009).
16. Y. Jiang, Z. Chen, Y. Han, P. Deb, H. Gao, S. Xie, P. Purohit, M. W. Tate, J. Park, S. M. Gruner, V. Elser, D. A. Muller, Electron ptychography of 2D materials to deep sub-ångström resolution. *Nature* **559**, 343–349 (2018).
17. O. L. Krivanek, M. F. Chisholm, V. Nicolosi, T. J. Pennycook, G. J. Corbin, N. Dellby, M. F. Murfitt, C. S. Own, Z. S. Szilagyi, M. P. Oxley, S. T. Pantelides, S. J. Pennycook, Atom-by-atom structural and chemical analysis by annular dark-field electron microscopy. *Nature* **464**, 571–574 (2010).
18. E. J. Kirkland, On the optimum probe in aberration corrected ADF-STEM. *Ultramicroscopy* **111**, 1523–1530 (2011).
19. G. T. Martinez, A. De Backer, A. Rosenauer, J. Verbeeck, S. Van Aert, The effect of probe inaccuracies on the quantitative model-based analysis of high angle annular dark field scanning transmission electron microscopy images. *Micron* **63**, 57–63 (2014).
20. W. Zhou, M. P. Oxley, A. R. Lupini, O. L. Krivanek, S. J. Pennycook, J.-C. Idrobo, Single atom microscopy. *Microsc. Microanal.* **18**, 1342–1354 (2012).
21. F. Lin, J. Jian, L. Ye, C. Jin, Effects of non-rotationally symmetric aberrations on the quantitative measurement of lattice positions in a graphene monolayer using high-resolution transmission electron microscopy. *Microscopy* **64**, 311–318 (2015).
22. C. Ophus, H. I. Rasool, M. Linck, A. Zettl, J. Ciston, Automatic software correction of residual aberrations in reconstructed HRTEM exit waves of crystalline samples. *Adv. Struct. Chem. Imaging* **2**, 15 (2017).
23. F. Lin, X. B. Ren, W. P. Zhou, L. Y. Zhang, Y. Xiao, Q. Zhang, H. T. Xu, H. Li, C. H. Jin, Exit-wave phase retrieval from a single high-resolution transmission electron microscopy image of a weak-phase object. *Micron* **114**, 23–31 (2018).
24. A. A. Govyadinov, A. Konečná, A. Chuvilin, S. Vélez, I. Dolado, A. Y. Nikitin, S. Lopatin, F. Casanova, L. E. Hueso, J. Aizpurua, R. Hillenbrand, Probing low-energy hyperbolic polaritons in van der Waals crystals with an electron microscope. *Nat. Commun.* **8**, 95 (2017).
25. S. Lopatin, B. Cheng, W.-T. Liu, M.-L. Tsai, J.-H. He, A. Chuvilin, Optimization of monochromated TEM for ultimate resolution imaging and ultrahigh resolution electron energy loss spectroscopy. *Ultramicroscopy* **184**, 109–115 (2018).

26. O. L. Krivanek, T. C. Lovejoy, N. Dellby, T. Aoki, R. W. Carpenter, P. Rez, E. Soignard, J. Zhu, P. E. Batson, M. J. Lagos, R. F. Egerton, P. A. Crozier, Vibrational spectroscopy in the electron microscope. *Nature* **514**, 209–212 (2014).
27. T. Miyata, M. Fukuyama, A. Hibara, E. Okunishi, M. Mukai, T. Mizoguchi, Measurement of vibrational spectrum of liquid using monochromated scanning transmission electron microscopy–electron energy loss spectroscopy. *Microscopy* **63**, 377–382 (2014).
28. A. Aljarb, Z. Cao, H.-L. Tang, J.-K. Huang, M. Li, W. Hu, L. Cavallo, L.-J. Li, Substrate lattice-guided seed formation controls the orientation of 2D transition-metal dichalcogenides. *ACS Nano* **11**, 9215–9222 (2017).
29. J. Barthel, Dr. Probe: A software for high-resolution STEM image simulation. *Ultramicroscopy* **193**, 1–11 (2018).
30. C. T. Koch, "Determination of Core Structure Periodicity and Point Defect Density Along Dislocations," thesis, Arizona State University (2002).
31. H. Yang, A. Giri, S. Moon, S. Shin, J.-M. Myoung, U. Jeong, Highly scalable synthesis of MoS_2 thin films with precise thickness control via polymer-assisted deposition. *Chem. Mater.* **29**, 5772–5776 (2017).
32. Y. Chen, S. Huang, X. Ji, K. Adepalli, K. Yin, X. Ling, X. Wang, J. Xue, M. Dresselhaus, J. Kong, B. Yildiz, Tuning electronic structure of single layer MoS_2 through defect and interface engineering. *ACS Nano* **12**, 2569–2579 (2018).
33. S. Kretschmer, H.-P. Komsa, P. Bøggild, A. V. Krasheninnikov, Structural transformations in two-dimensional transition-metal dichalcogenide MoS_2 under an electron beam: Insights from first-principles calculations. *J. Phys. Chem. Lett* **8**, 3061–3067 (2017).
34. Y.-C. Lin, D. O. Dumcenco, Y.-S. Huang, K. Suenaga, Atomic mechanism of the semiconducting-to-metallic phase transition in single-layered MoS_2. *Nat. Nanotechnol.* **9**, 391–396 (2014).
35. J.-K. Huang, J. Pu, C.-L. Hsu, M.-H. Chiu, Z.-Y. Juang, Y.-H. Chang, W.-H. Chang, Y. Iwasa, T. Takenobu, L.-J. Li, Large-area synthesis of highly crystalline WSe_2 monolayers and device applications. *ACS Nano* **8**, 923–930 (2013).
36. H. Li, P. Li, J.-K. Huang, M.-Y. Li, C.-W. Yang, Y. Shi, X.-X. Zhang, L.-J. Li, Laterally stitched heterostructures of transition metal dichalcogenide: Chemical vapor deposition growth on lithographically patterned area. *ACS Nano* **10**, 10516–10523 (2016).
37. K. Momma, F. Izumi, *VESTA 3* for three-dimensional visualization of crystal, volumetric and morphology data. *J. Appl. Cryst.* **44**, 1272–1276 (2011).

Acknowledgments: A.A. acknowledges X. Zhang for the brief mentorship during the transition period. **Funding:** V.T., A.A., and J.-H.F. are indebted to the support from the King Abdullah University of Science and Technology (KAUST) Office of Sponsored Research (OSR) under award no. OSR-2018-CARF/CCF-3079. V.T. acknowledges the support from User Proposals (nos. 5067 and 5424) at the Molecular Foundry, Lawrence Berkeley National Laboratory, supported by the Office of Basic Energy Sciences, of the U.S. Department of Energy under contract no. DE-AC02-05CH11231. The financial support from the Deutsche Forschungsgemeinschaft (DFG) via the CRC 1073 project Z02 and B02 is acknowledged. **Author contributions:** A.A. and S.L. found the phenomenon. S.L. and V.R. proposed the explanation. V.R. and T.M. conducted the simulations. S.L. designed and performed the STEM and EELS experiments. A.A., J.-H.F., and Y.W. prepared the samples and performed the optical measurements. M.H. performed the XPS measurements. S.L., A.A., V.R, Y.H., L.-J.L., and V.T. wrote the manuscript. V.T. and L.-J.L. supervised the project. All authors discussed and commented on the manuscript. **Competing interests:** The authors declare that they have no competing interests. **Data and materials availability:** All data are reported in the main text and the Supplementary Materials. Additional data related to this paper may be requested from the authors.

Submitted 5 April 2020
Accepted 28 July 2020
Published 9 September 2020
10.1126/sciadv.abb8431

Citation: S. Lopatin, A. Aljarb, V. Roddatis, T. Meyer, Y. Wan, J.-H. Fu, M. Hedhili, Y. Han, L.-J. Li, V. Tung, Aberration-corrected STEM imaging of 2D materials: Artifacts and practical applications of threefold astigmatism. *Sci. Adv.* **6**, eabb8431 (2020).